

DOI: 10.1002/((please add manuscript number))

**Article type: Communication**

## **Charge Transport Modulation of a Flexible Quantum Dot Solar Cell using a Piezoelectric Effect**

*Yuljae Cho, Paul Giraud, Bo Hou, Young-Woo Lee, John Hong, Sanghyo Lee, Sangyeon Pak, Juwon Lee, Jae Eun Jang, Stephen M. Morris, Jung Inn Sohn<sup>\*</sup>, SeungNam Cha<sup>\*</sup>, and Jong Min Kim*

Y. Cho, P. Giraud, Dr. B. Hou, Dr. Y.-W. Lee, J. Hong, Dr. S. Lee, S. Pak, J. Lee, Prof. S. M. Morris, Dr. J. I. Sohn, Prof. S. Cha

Department of Engineering Science, University of Oxford, Parks Road, Oxford, OX1 3PJ, United Kingdom

E-mail: [seungnam.cha@eng.ox.ac.uk](mailto:seungnam.cha@eng.ox.ac.uk), [junginn.sohn@eng.ox.ac.uk](mailto:junginn.sohn@eng.ox.ac.uk)

Prof. J. E. Jang

Department of Information and Communication Engineering, Daegu Gyeongbuk Institute of Science and Technology, Daegu 711-873, Republic of Korea

Prof. J. M. Kim

Department of Engineering, University of Cambridge, 9 JJ Thomson Avenue, Cambridge CB3 0FA, United Kingdom

**Keywords:** lead sulfide quantum dots, flexible solar cell, piezoelectric effect, charge transport modulation

**Abstract:** Colloidal quantum dots are promising materials for flexible solar cells as they have a large absorption coefficient at visible and infrared wavelengths, a band gap that can be tuned across the solar spectrum, and compatibility with solution processing. However, the performance of flexible solar cells can be degraded by the loss of charge carriers due to recombination pathways that exist at a junction interface as well as the strained interface of the semiconducting layers. The modulation of the charge carrier transport by the piezoelectric effect is an effective way of resolving and improving the inherent material and structural defects. By inserting a porous piezoelectric P(VDF-TrFE) layer so as to generate a converging electric field, it is possible to modulate the junction properties and consequently enhance the charge carrier behavior at the junction. In this study, we show that due to a reduction in the recombination and an improvement in the carrier extraction, a 38% increase in the current

density along with a concomitant increase of 37% in the power conversion efficiency of flexible quantum dots solar cells can be achieved by modulating the junction properties using the piezoelectric effect.

Flexible solar cells have emerged as promising energy sources for a variety of advanced technological applications such as electronic textiles, artificial skin, and portable devices. This is because solar cells that are conformable can be easily integrated into various shapes and surfaces.<sup>[1,2]</sup> To date, considerable effort has already been devoted to realizing high efficiency flexible solar cells. As an example, a recent development has been the demonstration of solution processible light absorption materials as well as highly flexible and stretchable electrodes that maintain the device performance on the application of strain/stress.<sup>[3-8]</sup> To further advance current flexible solar cell technologies, however, a larger absorption efficiency is required so as to have a high solar cell efficiency with a photoactive layer that is as thin as possible in order to attain a high degree of flexibility. In this regard, colloidal quantum dots (QDs) are one of the most promising materials as they have been shown to exhibit a high light absorption coefficient, a tunable band gap across the solar spectrum, and are solution processible.<sup>[9,10]</sup>

Amongst the various types of QD materials, lead sulfide (PbS) QDs are considered to be one of the most attractive materials for solar cell applications because of their large Bohr radius, wide tuning range of the bandgap, low material cost and air stability.<sup>[11]</sup> As a result of these properties, PbS QD solar cells (QDSCs) have demonstrated a remarkable improvement in the efficiency when used in conventional, rigid solar cell architectures.<sup>[12]</sup> However, there is still room for further improvement in the QDSC performance. For example, by addressing factors such as the relatively low built-in potential, the excessive surface trap sites and interfaces, which cause an open circuit voltage ( $V_{oc}$ ) deficit, and the low charge carrier dissociation and collection rate, it has been possible to enhance the performance of the solar cells.<sup>[13-16]</sup> In particular, the

heterojunction between the electron transport layer (ETL) and the PbS QD layer plays a key role in governing the overall performance of the PbS QDSCs because charge trapping and recombination occurs much faster at this heterojunction than at other locations between and within the PbS QD layers.<sup>[17]</sup> To reduce the charge recombination at the interfaces, various strategies have been considered, such as engineering the energy band levels as well as the employment of a buffer layer.<sup>[18-20]</sup> However, flexible QDSCs are more susceptible to the loss of charge carriers at the junction due to recombination pathways that arise from the straining of the semiconducting layers during the fabrication process, which is a major limitation that has to be dealt with for an improvement in the performance of flexible QDSCs to be realised.<sup>[9][10]</sup> Therefore, fundamental strategies for structurally and actively controlling the junction properties are required to boost extraction and reduce the recombination of photo-generated charges in order to advance the performance of flexible QDSCs.

Towards this end, we have employed a porous piezoelectric poly(vinylidene fluoride-trifluoroethylene) P(VDF-TrFE) polymer layer between a zinc oxide (ZnO) ETL and a PbS QD heterojunction in a flexible QDSC. Through the active control of strain/stress of the flexible form factors, the inserted porous P(VDF-TrFE) layer generates a piezoelectric potential which modulates the junction properties and consequently changes the behavior of the charge carriers. As a result, the modulated electric field at the junction effectively extracts the photo-generated charges and reduces radiative recombination, resulting in enhanced current density ( $J_{sc}$ ) and consequently a higher power conversion efficiency (PCE) in the flexible solar cells.

**Figure 1a** shows a schematic structure and photographs of the flexible PbS QDSCs that were treated with tetrabutylammonium iodide (TBAI) and 1,2-ethanedithiol (EDT) ligands.<sup>[12,21]</sup> The absorption peak and high resolution transmission electron microscopy (HRTEM) analysis revealed that the bandgap of the PbS QDs was 1.23 eV and the QDs showed

the typical rock-salt cubic characteristics as indicated by the indexed lattice fringes ((200) and (100)) in Figure 1b, respectively. A P(VDF-TrFE) layer was inserted between the ZnO ETL and the PbS QD layers so as to modulate the junction properties by introducing a piezoelectric potential. Further details of the solar cell fabrication method are provided in the experimental section. In spite of the high piezoelectric coefficient and flexibility of the P(VDF-TrFE) film, the insulating nature of the polymer restricts efficient transport of the charge carriers. The use of a conjugated structure, which was a mixture of a semiconducting material with the polymer, has been reported previously. However, it was noted that the diverging and non-uniform electric field that was caused by the randomly distributed P(VDF-TrFE) polymer limited the efficient dissociation and extraction of the charge carriers.<sup>[22-24]</sup> In order to generate a converging and uniform electric field together with secured charge carrier paths, a P(VDF-TrFE) layer with a porous structure was deposited on top of the ZnO ETL layer as shown by the atomic force microscopy (AFM) image in Figure 1c (left). Afterwards, the porous P(VDF-TrFE) layer was thermally annealed to form a piezoelectric  $\beta$ -phase as shown in Figure 1c (top right) which exhibits the most favorable piezoelectric properties in comparison to the other phases of P(VDF-TrFE) polymers.<sup>[25,26]</sup> The  $\beta$ -phase P(VDF-TrFE) layer in the flexible PbS QDSC generated a piezoelectric potential under mechanical vibration at a frequency of 30 Hz as shown in Figure 1c (bottom right and Supplementary Figure S1). In addition, the transmittance of the ZnO-P(VDF-TrFE) layer displayed a similar transparency to that of the ZnO ETL alone as shown in Figure 1d, which indicates that there will be negligible light loss and performance degradation because of the addition of the P(VDF-TrFE) layer.

Cross-sectional illustrations describing the effect of modulation of the piezoelectric potential on the flexible PbS QDSCs are shown in Figure 2 along with a 3D plan views of a porous P(VDF-TrFE) layer, which are also shown in Supplementary Figures S2a and b. In addition, the evolution of the morphology following deposition of a QD layer on the porous

P(VDF-TrFE) structure was recorded using an AFM, which revealed that the porous structure became fully filled with QDs as shown in Supplementary Figure S3. As revealed by XRD measurements in Figure 1c, a  $\beta$ -phase P(VDF-TrFE) layer exhibits a certain molecular orientation (Supplementary Figure S2c) in such a way that negative fluorine (F) atoms align to one side of the backbone and positive hydrogen atoms align to the other side. As a result, a P(VDF-TrFE) layer exhibits a spontaneous polarization.<sup>[27,28]</sup> When the spatially symmetrical arrangement of a  $\beta$ -crystalline P(VDF-TrFE) backbone chain becomes asymmetry through the application of strain, the induced polarization of the P(VDF-TrFE) increases (or decreases) because the magnitude of the polarization is proportional to the distance between the F and H atoms.<sup>[27,29]</sup> This structural change in the P(VDF-TrFE) molecules causes the magnitude of the piezoelectric potential to be modulated by the application of mechanical stress/strain as shown in Supplementary Figures S2(d) and (e), which in turn enables the behavior of the charge carriers in a flexible QDSC to be modulated.

As shown in Figures 2a and b, the application of a compressive strain to the flexible PbS QDSC induces a piezoelectric potential, which leads to the formation of a steep electric potential, i.e. higher electric field, at the junction as a result of the modulation of the space charge region compared to a QDSC that is not subjected to any strain (no strain). Consequently, exciton dissociation and charge carrier extraction are enhanced at the hetero-junction. On the contrary, exciton dissociation and charge carrier extraction are diminished when a gradual distribution of the electric potential, i.e. lower electric field, was formed at the junction under tensile strain as shown in Figure 2c.

In order to understand the changes in the junction properties, such as the distribution of the electric potential and the space charge region at the heterojunction that results from the piezoelectric potential under the application of strain, we carried out simulations with the

COMSOL Multiphysics software. It is worth noting that a ZnO layer which was spin-coated from a solution phase did not exhibit a piezoelectric potential as shown in Supplementary Figure S1c due to the random orientation of the ZnO nanoparticles and thus only a porous P(VDF-TrFE) layer was chosen as the piezoelectric material for the simulation. Details of the parameters and equations used for the simulations are described in Supplementary Information I. As shown in Figure 3a, the distribution of the electric potential across the ZnO-PbS QD layers can be modulated by the application of compressive and tensile strain. The slope of the electric potential distribution across the junction became steeper when the compressive strain was applied to the devices, which enhanced exciton dissociation and charge extraction. On the other hand, the application of tensile strain resulted in a gradual electric potential distribution at the junction and consequently exciton dissociation and charge extraction were decreased. Further, the enhanced electric field introduced by the strain (no strain to compressive 1.25%) at the hetero-junction (100 ~ 120 nm) was approximately 33% (from  $7.5 \times 10^6$  (no strain) to  $10^7$  V/m (compressive 1.25%)).

The color changes at the heterojunction in Figure 3b highlight the modulation of the electric potential due to the application of compressive and tensile strains. Under compressive strain, charge carriers were drawn into the pores in the P(VDF-TrFE) layer and were effectively transported to the ZnO layer as described by the direction of the arrows. In contrast, it was observed that the formation of the diverging and weak distribution of the electric potential for a tensile strain could not effectively transport photo-generated charges to the ZnO layer as shown in Figure 3b, which led to severe charge carrier loss at the heterojunction. Also, the size of the arrows, which are proportional to the amplitude of the electric field at each point, describes the modulation of the electric potential/field by compressive and tensile strain. This modulation of the electric potential/field is also attributed to the modulation of the space charge region by the induced piezoelectric potential as shown in Figure 3c, where colored regions of

red and blue indicate the density of positive and negative space charges, respectively. The formation of a narrow space charge region resulted in the generation of a steep distribution in the electric potential at the heterojunction whereas the formation of a wide space charge region ended up with the generation of a gradual potential change as illustrated in Figure 3b (Equation (1) for potential distribution at semiconducting junction in supplementary information II). The simulation results highlight that the modulated piezoelectric potential that is caused by simply changing the directions of the strain imposed on the piezoelectric layer are able to modulate the space charge region and also the potential distribution, which can facilitate or hinder the transport of charge carriers.

Experimental verification of the modulation in the charge carrier transport that is caused by the piezoelectric potential was then carried out by fabricating flexible QDSCs with the structure presented in Figure 1a. As shown in Figure 4a, it is evident that the P(VDF-TrFE) layer without the porous structure restricted the transport of photo-generated charge carriers due to the insulating nature of the P(VDF-TrFE) layer, which resulted in a poor solar cell performance compared to that of the flexible QDSC with a porous P(VDF-TrFE) layer (Supplementary Table S1). The thicknesses of both P(VDF-TrFE) layers were approximately 20 nm and the porous structures were fabricated by controlling the evaporation rate as well as the concentration of the P(VDF-TrFE) solution as shown in Figure S4. The performances of QDSCs with a porous P(VDF-TrFE) layer were optimized and the optimized conditions were used for all QDSCs unless otherwise stated as shown in Supplementary Figure S5 and Table S2. More details about the fabrication of a porous structure P(VDF-TrFE) layer are described in the Experimental Section. It is noted that the enhanced performance of the flexible QDSC with a porous P(VDF-TrFE) layer compared to the QDSC with only a ZnO layer at no applied strain in Figure 4c (0 strain column) is due to the spontaneous polarization of the electric dipoles in the P(VDF-TrFE), which was repeatedly observed in PbS QDSCs based on a glass substrate

that prohibits any strain as shown in Supplementary Figure S6 and Table S3.<sup>[18]</sup> This result emphasizes that the porous P(VDF-TrFE) layer facilitates charge carrier transport and improves the performance of a QDSC via the piezoelectric effect; without this effect the layer would severely deteriorate the performance due to the insulating nature of the polymer.

The effect of the piezoelectric potential on the solar cell performance was investigated by applying compressive or tensile strain to the flexible QDSCs with the porous P(VDF-TrFE) layer. The applied strain was carefully controlled by a micrometer that was attached to a bending machine as shown in the bottom inset of Figure 4b. A noticeable modulation in  $J_{sc}$ , on the order of approximately 37% (from 14.18 to 19.53 mAcm<sup>-2</sup>), was observed at various strain rates as shown in Figure 4b and Supplementary Table S1. This is attributed to an increase (or decrease) in the exciton dissociation and charge extraction as the applied electric potential at the junction was increased (decreased) by the application of larger compressive (or tensile) strain as illustrated in Figure 3. Also, it was observed that the performance of the solar cell were maintained under repeated strain that was applied by changing the direction of strain, compressive to tensile or tensile to compressive, as shown in Supplementary Figure S7. The experimental result was consistent with the theoretical simulations, which predicted a modulation of the  $J_{sc}$  (performed using the COMSOL Multiphysics software) as shown in Supplementary Figure S8 and also in the equation for the exciton dissociation rates as a function of the applied electric potential in Supplementary Information II.<sup>[24,30]</sup> However, a modulation of  $V_{oc}$  was not noticeable compared to that observed for  $J_{sc}$  because the induced piezoelectric potential was effective only on the heterojunction and adjacent area, and did not affect the quasi-Fermi level of the whole solar cell system. A similar phenomenon was also observed in solar cells that exploited ferroelectricity. As a result of the  $J_{sc}$  modulation, the PCE values were also found to be substantially altered, for example,  $\Delta PCE \approx 1.37\%$  (from 3.68% to 5.05%), as depicted in Figure 4c (red), which indicates that the performance of the solar cell is controllable

by simply adjusting the strain rates applied to the flexible QDSC. However, for the QDSC with only a ZnO layer (i.e. without the presence of a piezoelectric effect) there was a negligible change in the performance when either compressive or tensile strain was applied, as shown in Figure 4c (black) and Supplementary Figure S9 and Table S4. It is worth stressing that the applied strain was kept relatively low (up to 1.25%) and thus the maximum change in distance between the QDSC and the light source was 2.5 mm which is a small change considering that a solar simulator is a collimated light source. A stark difference in the modulation of the PCE in two types of QDSCs (Figure 4c) suggests that the small distance change that arises through a bending of the QDSCs had a negligible effect on the performance enhancement, which supports our finding that the modulation of the charge carrier behavior and the distribution of the potential at the hetero-junction was caused by a piezoelectric effect of the porous P(VDF-TrFE) layer. The average values for the parameters from 15 separate flexible QDSCs are shown in Table 1. When a higher strain was applied, however, we observed degradation in the solar cell performance, which was due to the formation of cracks on the QD films as demonstrated in Supplementary Figure S10 and Table S5. The strain rate was calculated based on the assumption that the applied strain is approximately equal to the strain of the outer surface of the flexible substrates because the thickness of the substrate (0.2 mm) is much larger than the total thickness of the QDSCs (500 nm).<sup>[32,33]</sup> The QDSCs with only a ZnO layer and with a ZnO-porous P(VDF-TrFE) layer showed reliable long-term stability under the application of mechanical vibrations with a linear motor (Supplementary Figure S1), which is the similar effect as straining the QDSC, for 2 hours (more than 210000 cycles) as shown in Supplementary Figure S11 and Table S6.

The efficient charge dissociation and extraction in the flexible QDSCs is also ascribed to the improved recombination kinetics, which were investigated by considering the dependence of the solar cell performance on the light intensity as well as the calculation of the ideality factor.

As shown in Figure 4d, the exponential factor  $\alpha$  that was calculated from a linear fit to  $J_{sc}$  as a function of light intensity on a logarithmic scale ( $J_{sc} \propto I^\alpha$ , where  $I$  is light intensity) shows clearly different aspects of the recombination dynamics. When compressive strain was applied to the QDSC the slope approached unity in contrast to that observed for no strain or tensile strain, which indicates that charge carriers are effectively transported prior to recombination, i.e. reduced non-radiative recombination.<sup>[34,35]</sup> Also, the calculated ideality factor was consistent with the result of the light intensity dependent solar cell performance. Upon the application of compressive strain on the QDSC, non-radiative recombination was suppressed whereas the opposite trend was observed with tensile strain as shown in Supplementary Table S8.<sup>[36-38]</sup> Ideality factors were calculated using equation (3) in Supplementary Information II and the dark saturation current shown in Supplementary Figure S12. Complementary results for the recombination dynamics revealed that the application of compressive strain led to improved charge carrier transport and reduced charge carrier loss, which resulted in the suppression of non-radiative recombination and thus an improvement of the overall flexible QDSC performance.

In summary, we have shown that the implementation of a piezoelectric polymer P(VDF-TrFE) layer with a porous structure on top of the ZnO layer in a flexible QDSC can result in an enhancement of the overall solar cell performance when subjected to compressive strain. Using a separate P(VDF-TrFE) film ensures that the semiconducting properties of the ZnO and PbS QD layers are retained, which could otherwise be degraded through the formation of conjugated structures such as a semiconducting ETL with P(VDF-TrFE). In accordance with the simulations, the piezoelectric potential that was generated by the strain/stress was found to increase the electric potential/field at the ZnO-PbS QD heterojunction due to a modulation of the space charge region. In addition, the performance of the flexible PbS QDSCs could be actively modulated by simply applying various strain rates, which is attributed to the enhanced

exciton dissociation, charge extraction and reduced trap-assisted recombination. Using this approach, an increase of the power conversion efficiency of approximately 37% was demonstrated.

## Experimental Section

*Solar cell fabrication:* Colloidal PbS QDs and ZnO nanoparticle solution were synthesized according to previously reported methods.<sup>[39]</sup> For the ZnO ETL layer, a solution of ZnO nanoparticles in chloroform was spin-coated onto patterned ITO that was either coated onto flexible or glass substrates at 3000 rpm for 40 seconds and thermally annealed at 130 °C for 2 hours in an oven. For the ZnO-P(VDF-TrFE) ETL layer, an additional solution of 0.5 – 1 wt% P(VDF-TrFE) was spin-coated on to the ZnO film at 3000 – 4000 rpm for 30 seconds and then thermally annealed at the same experimental conditions. 2-Butanon, which was chosen as it has a relatively low boiling point that is advantageous for drying the solvent quickly, was used as a solvent for dissolving P(VDF-TrFE). Various spin-coating speeds were used from 3000 to 5000 rpm and the optimized conditions were obtained for a concentration of 0.5 wt% with a spin-coating speed of 3000 rpm. Afterwards, PbS QD layers were spin-coated at 2500 rpm. For the solid-state ligand exchange of the PbS QD layers, a tetrabutylammonium iodide (TBAI) solution with a concentration of 10 mgmL<sup>-1</sup> was loaded and held for 30 seconds, which was followed by a washing process with methanol. 1,2-Ethanedithiol (EDT) treated QD layer (0.02 vol% in acetonitrile) was prepared by the same procedure as the TBAI except that acetonitrile was used as the solvent for the washing procedure. All QDSCs consisted of 10 layers of TBAI and 2 layers of EDT structures, unless stated otherwise. Gold electrodes with 100 nm thickness were deposited using thermal evaporation.

*Solar cell characterization:* Solar cell measurements were performed using a source meter (Keithley 4200-SCS) and a solar simulator (LOT-Quantum Design) with an AM 1.5 G filter ( $100 \text{ mWcm}^{-2}$ ). The standard cell (Rera system) was measured before solar cell measurements. All measurements were carried out in ambient air at room temperature. To specify the size of the active area, we used a mask pattern with a size of  $0.018 \pm 0.001 \text{ cm}^2$ .

### Supporting Information

Supporting Information is available from the Wiley Online Library or from the author.

### Acknowledgements

This work was supported by the International Collaborative Energy Technology R&D Program of the Korea Institute of Energy Technology Evaluation and Planning (KETEP), granted financial resource from the Ministry of Trade, Industry & Energy, Republic of Korea (20142020103970) and National Research Foundation (NRF) of Korea (2015M2A2A6A02045252).

Received: ((will be filled in by the editorial staff))

Revised: ((will be filled in by the editorial staff))

Published online: ((will be filled in by the editorial staff))

### References

- [1] M. Kaltenbrunner, M. S. White, E. D. Głowacki, T. Sekitani, T. Someya, N. S. Sariciftci, S. Bauer, *Nat. Commun.* **2012**, 3, 770.
- [2] K. Li, H. Zhen, L. Niu, X. Fang, Y. Zhang, R. Guo, Y. Yu, F. Yan, H. Li, Z. Zheng, *Adv. Mater.* **2014**, 26, 7271.
- [3] J. Nam, Y. Lee, W. Choi, C. S. Kim, H. Kim, J. Kim, D. Kim, S. Jo, *Adv. Energy Mater.* **2016**, 1601269.
- [4] Q. Lin, L. Lu, M. M. Tavakoli, C. Zhang, G. C. Lui, Z. Chen, X. Chen, L. Tang, D. Zhang, Y. Lin, *Nano Energy* **2016**, 22, 539.

- [5] J. H. Heo, M. H. Lee, H. J. Han, B. R. Patil, J. S. Yu, S. H. Im, *J. Mater. Chem. A* **2016**, 4, 1572.
- [6] S. Savagatrup, A. D. Printz, T. F. O'Connor, A. V. Zaretski, D. Rodriguez, E. J. Sawyer, K. M. Rajan, R. I. Acosta, S. E. Root, D. J. Lipomi, *Energy Environ. Sci.* **2015**, 8, 55.
- [7] J. Ham, W. J. Dong, J. Y. Park, C. J. Yoo, I. Lee, J. Lee, *Adv. Mater.* **2015**, 27, 4027.
- [8] K. Poorkazem, D. Liu, T. L. Kelly, *J. Mater. Chem. A* **2015**, 3, 9241.
- [9] I. J. Kramer, G. Moreno-Bautista, J. C. Minor, D. Kopilovic, E. H. Sargent, *Appl. Phys. Lett.* **2014**, 105, 163902.
- [10] Y. Li, L. Wei, C. Wu, C. Liu, Y. Chen, H. Liu, J. Jiao, L. Mei, *J. Mater. Chem. A* **2014**, 37, 15546.
- [11] F. W. Wise, *Acc. Chem. Res.* **2000**, 33, 773.
- [12] X. Lan, O. Voznyy, F.P. García de Arquer, M. Liu, J. Xu, A. H. Proppe, G. Walters, F. Fan, H. Tan, M. Liu, Z. Yang, S. Hoogland, E.H. Sargent, *Nano Lett.* **2016**, 16, 4630.
- [13] B. Kim, D. C. Neo, B. Hou, J. B. Park, Y. Cho, N. Zhang, J. Hong, S. Pak, S. Lee, J. I. Sohn, *ACS Appl. Mater. Interfaces* **2016**, 8, 13902.
- [14] G. W. Hwang, D. Kim, J. M. Cordero, M. W. Wilson, C. M. Chuang, J. C. Grossman, M. G. Bawendi, *Adv. Mater.* **2015**, 27, 4481.
- [15] C. M. Chuang, A. Maurano, R. E. Brandt, G. W. Hwang, J. Jean, T. Buonassisi, V. Bulović, M. G. Bawendi, *Nano Lett.* **2015**, 15, 3286.
- [16] J. Hong, B. Hou, J. Lim, S. Pak, B-S. Kim, Y. Cho, J. Lee, Y-W. Lee, P. Giraud, S. Lee, J. B. Park, S. M. Morris, H. J. Snaith, J. I. Sohn, S. Cha, J. M. Kim, *J. Mater. Chem. A* **2016**, 4, 18769.
- [17] R. Azmi, S. Oh, S. Jang, *ACS Energy Lett.* **2016**, 1, 100.
- [18] G. Kim, F.P. García de Arquer, Y. J. Yoon, X. Lan, M. Liu, O. Voznyy, Z. Yang, F. Fan, A. H. Ip, P. Kanjanaboos, S. Hoogland, J.Y. Kim, E.H. Sargent, *Nano lett.* **2015**, 15, 7691.

- [19] P. H. Rekemeyer, S. Chang, C. M. Chuang, G. W. Hwang, M. G. Bawendi, S. Gradečak, *Adv. Energy Mater.* **2016**, 6, 1600848.
- [20] X. Zhang, E. M. Johansson, *J. Mater. Chem. A* **2017**, 5, 303.
- [21] C. H. Chuang, P. R. Brown, V. Bulovic, M. G. Bawendi, *Nat. Mater.* **2014**, 13, 796.
- [22] K. Shin, T. Y. Kim, G. C. Yoon, M. K. Gupta, S. K. Kim, W. Seung, H. Kim, S. Kim, S. Kim, *Adv. Mater.* **2014**, 27, 5619.
- [23] S. B. Jo, M. Kim, D. H. Sin, J. Lee, H. G. Kim, H. Ko, K. Cho, *Adv. Energy Mater.* **2015**, 5, 1500802.
- [24] K. S. Nalwa, J. A. Carr, R. C. Mahadevapuram, H. K. Kodali, S. Bose, Y. Chen, J. W. Petrich, B. Ganapathysubramanian, S. Chaudhary, *Energy Environ. Sci.* **2012**, 5, 7042.
- [25] Y. Cho, J. B. Park, B. Kim, J. Lee, W. Hong, I. Park, J. E. Jang, J. I. Sohn, S. Cha, J. M. Kim, *Nano Energy* **2015**, 16, 524.
- [26] G. Ni, Y. Zheng, S. Bae, C. Y. Tan, O. Kahya, J. Wu, B. H. Hong, K. Yao, B. Ozyilmaz, *ACS Nano* **2012**, 6, 3935.
- [27] J. Lee, K. Y. Lee, B. Kumar, N. T. Tien, N. Lee, S. Kim, *Energy Environ. Sci.* **2013**, 6, 169.
- [28] J. Lee, K. Y. Lee, M. K. Gupta, T. Y. Kim, D. Lee, J. Oh, C. Ryu, W. J. Yoo, C. Kang, S. Yoon, *Adv. Mater.* **2014**, 26, 765.
- [29] K. S. Ramadan, D. Sameoto, S. Evoy, *Smart Mater. Struct.* **2014**, 23, 033001.
- [30] Y. Yuan, T. J. Reece, P. Sharma, S. Poddar, S. Ducharme, A. Gruverman, Y. Yang, J. Huang, *Nat. Mater.* **2011**, 10, 296.
- [31] S. Nam, J. Seo, S. Woo, W. H. Kim, H. Kim, D. D. Bradley, Y. Kim, *Nat. Commun.* **2015**, 6, 8929.
- [32] S. Liu, Q. Liao, S. Lu, Z. Zhang, G. Zhang, Y. Zhang, *Adv. Funct. Mater.* **2016**, 26, 1347.
- [33] R. Yang, Y. Qin, L. Dai, Z. L. Wang, *Nat. Nanotechnol.* **2009**, 4, 34.

- [34] D. Zhao, M. Sexton, H.-Y. Park, G. Baure, J. C. Nino, F. So, *Adv. Energy Mater.* **2015**, 5, 1401855.
- [35] H. Aqoma, N. Barange, I. Ryu, S. Yim, Y. R. Do, S. Cho, D. Ko, S. Jang, *Adv. Funct. Mater.* **2015**, 25, 6241.
- [36] D. Bozyigit, W. M. Lin, N. Yazdani, O. Yarema, V. Wood, *Nat. Commun.* **2015**, 6, 6180.
- [37] W. Yoon, J. E. Boercker, M. P. Lumb, D. Placencia, E. E. Foos, J. G. Tischler, *Sci. Rep.* **2013**, 3, 2225.
- [38] D. Zhitomirsky, O. Voznyy, L. Levina, S. Hoogland, K. W. Kemp, A. H. Ip, S. M. Thon, E. H. Sargent, *Nat. Commun.* **2014**, 5, 3803.
- [39] B. Hou, Y. Cho, B. S. Kim, J. Hong, J. B. Park, S. J. Ahn, J. I. Sohn, S. Cha, J. M. Kim, *ACS Energy Lett.* **2016**, 1, 834.

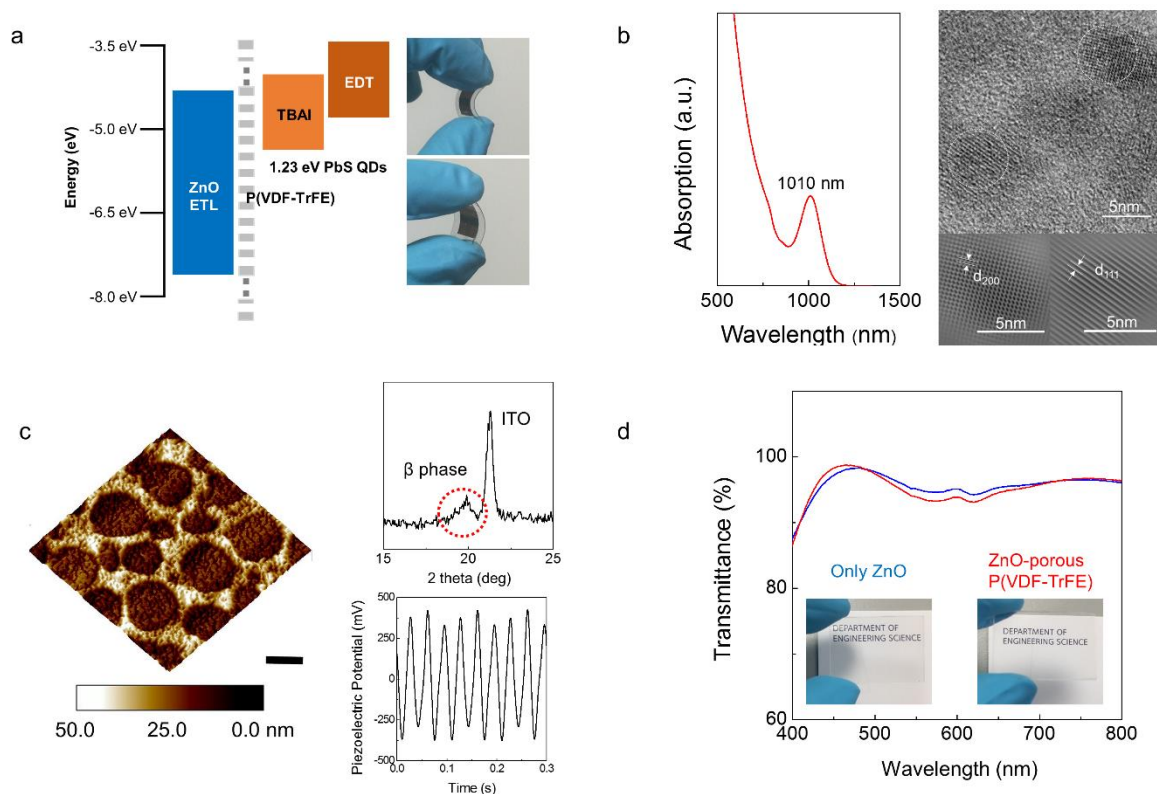


**Figure 1.** (a) Energy structure and photographs of the flexible PbS QDSC. (b) Absorption peak of the synthesized PbS QDs and corresponding TEM (and HRTEM) images (c) AFM image of a porous-structured P(VDF-TrFE) film at a scan size of  $10 \times 10 \mu\text{m}$  (scale bar:  $2 \mu\text{m}$ ), the formation of the  $\beta$ -phase P(VDF-TrFE) film measured by XRD (top right), and the generation of a piezoelectric potential by the flexible PbS QDSC (bottom right). (d) Transmittance of only ZnO (blue) and ZnO-porous P(VDF-TrFE) ETL (red).

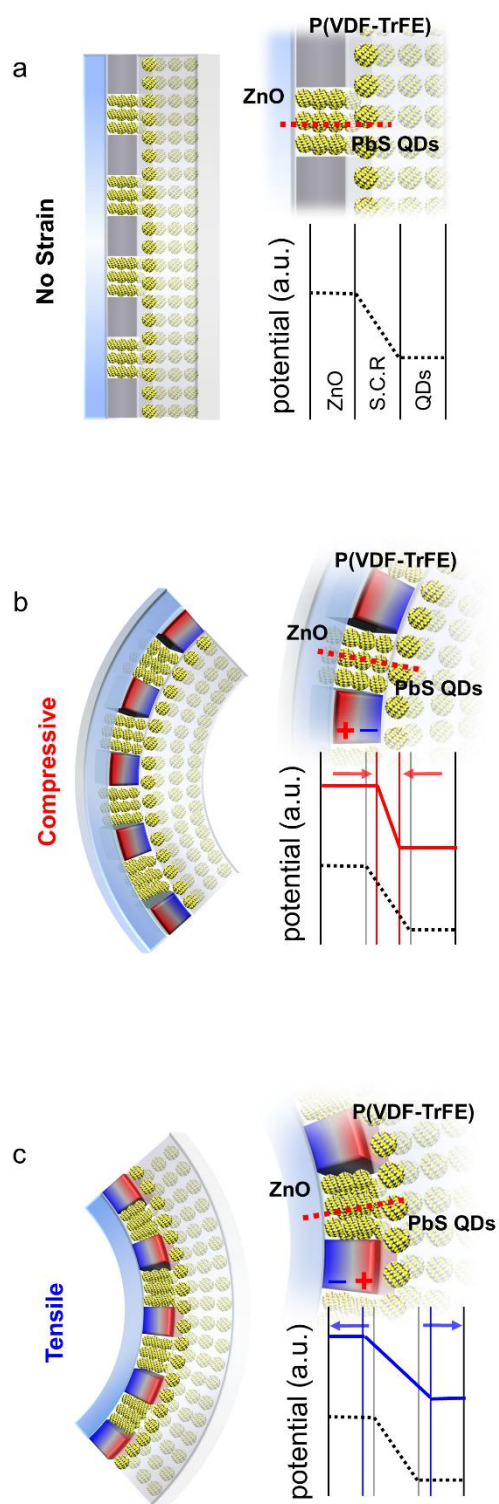


**Figure 2.** Illustration highlighting the modulation of the junction properties through changes in the piezoelectric potential in the flexible PbS QDSC (a) with no strain and upon the application of (b) a compressive and (c) a tensile strain, where S.C.R indicates the space charge region and the red dotted line indicates the line on which the potential profile is read.

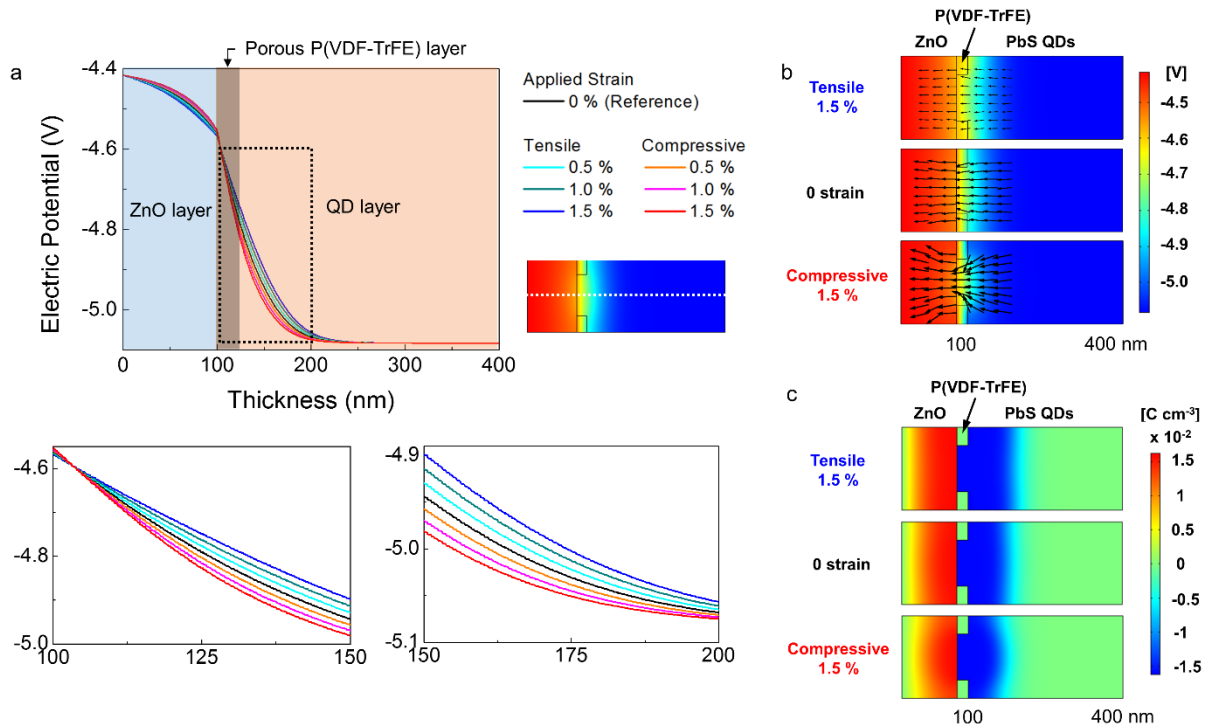


**Figure 3.** (a) Cross-sectional view of the distribution of the electric potential at the ZnO-PbS QD hetero-junction, where the potential over the region from 100 to 200 nm was enlarged in the lower plots; the potential was read at the position as indicated by the white dotted line for different applied strain amplitudes. (b) 2-dimensional distribution of the electric potential at the junction for 1.5% tensile, 0 and 1.5% compressive strain, respectively. The arrows indicate the direction of electron flow and the size of the arrows indicates the intensity of the electric field at that point. (c) 2-dimensional representation of the space charge region for 1.5% tensile, 0 and 1.5% compressive strain, respectively, where the red color describes a density of positively bound charges and the blue color a density of negatively bound charges.

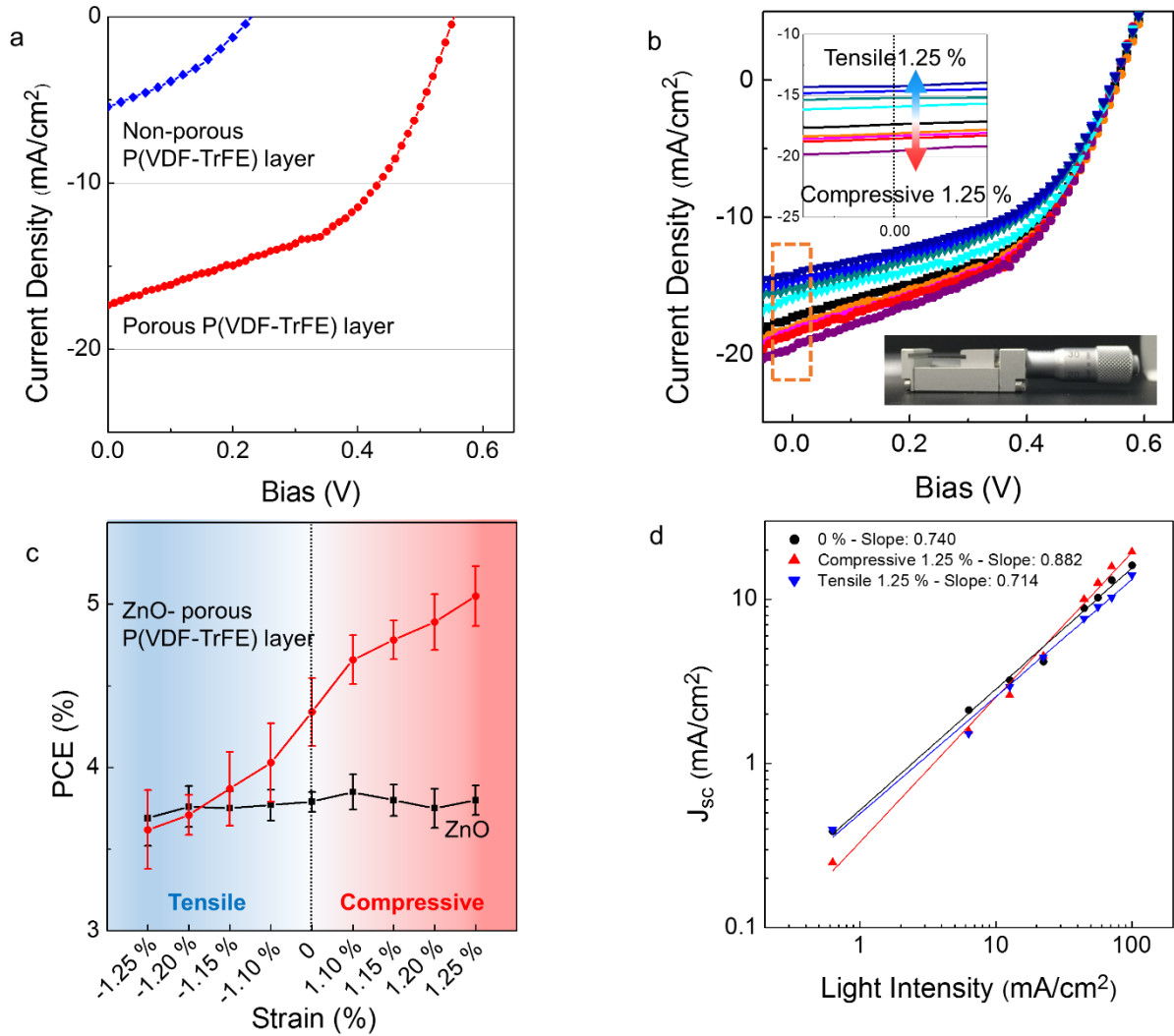


**Figure 4.** (a) Performance of the flexible QDSC measured in the absence of any strain where the blue curve is for the ZnO-P(VDF-TrFE) sample without a porous polymer structure and the red curve represents the ZnO-P(VDF-TrFE) sample with a porous structure. (b) J-V curves at no strain as well as compressive and tensile strain ranging from 1.10 to 1.25%; top left inset shows enlarged  $J_{sc}$  level for different strain amplitudes, and bottom right inset shows the bending machine with a micrometer. (c) Modulation of the power conversion efficiency of the ZnO-P(VDF-TrFE) layer with a porous structure (red) and the QDSC with only a ZnO layer (black) with respect to the application of a tensile and compressive strain. (d) Dependence of the short circuit current,  $J_{sc}$ , on the light intensity for 0, 1.25% compressive, and 1.25% tensile strain. The solid lines are linear fits to the data.

**Table 1.** Average value of the solar cell parameters taken from 15 separate devices at 1.25% compressive, 0, and 1.25% tensile strain as shown in Figure 4c.

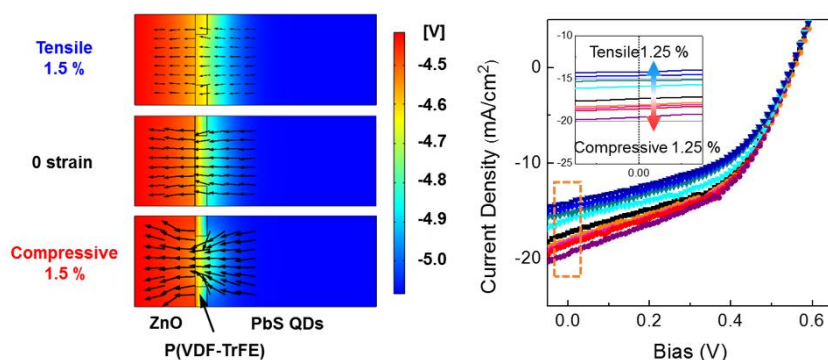
Sample	Strain (%)	$V_{oc}$ (V)	$J_{sc}$ (mAcm <sup>-2</sup> )	FF	PCE (%)
<b>Figure 4c</b>	Compressive 1.25	$0.55 \pm 0.0101$	$19.53 \pm 0.7168$	$0.47 \pm 0.0170$	<b><math>5.05 \pm 0.1840</math></b>
	Compressive 1.20	$0.55 \pm 0.0092$	$18.68 \pm 0.3226$	$0.48 \pm 0.0189$	<b><math>4.91 \pm 0.1696</math></b>
	Compressive 1.15	$0.55 \pm 0.01$	$18.23 \pm 0.3830$	$0.48 \pm 0.0140$	<b><math>4.80 \pm 0.1184</math></b>
	Compressive 1.10	$0.55 \pm 0.01$	$17.79 \pm 0.2548$	$0.48 \pm 0.0192$	<b><math>4.68 \pm 0.1496</math></b>
	0	$0.55 \pm 0.0074$	$17.40 \pm 0.3274$	$0.47 \pm 0.0250$	<b><math>4.50 \pm 0.2076</math></b>
	Tensile 1.10	$0.55 \pm 0.01$	$15.84 \pm 0.4364$	$0.47 \pm 0.0210$	<b><math>4.09 \pm 0.2392</math></b>
	Tensile 1.15	$0.55 \pm 0.0095$	$15.28 \pm 0.2328$	$0.47 \pm 0.0158$	<b><math>3.95 \pm 0.2264</math></b>
	Tensile 1.20	$0.55 \pm 0.0074$	$14.77 \pm 0.2682$	$0.47 \pm 0.0155$	<b><math>3.80 \pm 0.1228</math></b>
	Tensile 1.25	$0.55 \pm 0.0079$	$14.18 \pm 0.3310$	$0.47 \pm 0.0190$	<b><math>3.68 \pm 0.2424</math></b>

**The table of contents: The modulation of the charge carrier transport in flexible PbS QD solar cells is demonstrated by harnessing the piezoelectric potential under compressive and tensile strain.** Modulation of the junction properties by the piezoelectric potential results in a 37% enhancement in the PCE, which is attributed to an efficient dissociation and extraction of the photo-generated charge carriers and a reduction in the non-radiative recombination.

**Keyword:** lead sulfide, quantum dots, flexible solar cells, piezoelectric effect, charge transport modulation

*Yuljae Cho, Paul Giraud, Bo Hou, Young-Woo Lee, John Hong, Sanghyo Lee, Sangyeon Pak, Juwon Lee, Jae Eun Jang, Stephen M. Morris, Jung Inn Sohn\*, SeungNam Cha\*, Jong Min Kim*

## Charge Transport Modulation of a Flexible Quantum Dot Solar Cell using a Piezoelectric Effect



## Supporting Information

### **Charge Transport Modulation of a Flexible Quantum Dot Solar Cell using a Piezoelectric Effect**

*Yuljae Cho, Paul Giraud, Bo Hou, Young-Woo Lee, John Hong, Sanghyo Lee, Sangyeon Pak, Juwon Lee, Jae Eun Jang, Stephen M. Morris, Jung Inn Sohn<sup>\*</sup>, SeungNam Cha<sup>\*</sup>, Jong Min Kim*

### Supporting Information I. Simulation designs.

Simulations were carried out using the COMSOL Multiphysics suite following a 2 step process. First, the surface charge densities  $\sigma$  (Ccm<sup>-2</sup>) of a PVDF slab (0.5 x 0.5 x 0.02  $\mu$ m) under strain were calculated using the piezoelectric module available with the software. The software solves the piezoelectric equations given in the strain charge form

$$\varepsilon = s_E S + d^T E$$

$$D = dS + \varepsilon_0 \varepsilon_r E,$$

where  $\varepsilon$ ,  $D$ ,  $S$  and  $E$  are the strain, electric displacement, stress, and electric field, respectively.

The material parameters  $s_E$ ,  $d$  and  $\varepsilon_r$  are the compliance, coupling matrix, and relative permittivity, respectively, taken as

$$d = \begin{bmatrix} 0 & 0 & 0 & 0 & 0 & 0 \\ 0 & 0 & 0 & 0 & 0 & 0 \\ 6 & 6 & -10 & 0 & 0 & 0 \end{bmatrix} \text{pCN}^{-1},$$

$$\varepsilon_r = \begin{bmatrix} 6.1 & 0 & 0 \\ 0 & 7.5 & 0 \\ 0 & 0 & 6.7 \end{bmatrix},$$

the values of  $s_E$  were taken from reference [1,2]. An initial strain tensor  $\varepsilon_0 = \begin{bmatrix} \varepsilon_x & 0 & 0 \\ 0 & 0 & 0 \\ 0 & 0 & 0 \end{bmatrix}$ , with

$\varepsilon_x$  varying from -1.5 to 1.5 was applied to account for the strain in the horizontal direction, inducing tensile and compressive strain of the slab following the sign of  $\varepsilon_x$ . The bottom of the slab was electrically grounded and two of its opposing edges were set as fixed constraints. The calculated values of the piezoelectric polarization,  $\sigma$ , at the top surface were then used in the second part of the study.

The solar cell was modelled with a 100 nm n-type ZnO layer doped at  $N_d = 10^{17} \text{ cm}^{-3}$ , a P(VDF-TrFE) film with a 20 nm thickness, a 84 nm hole size, and a 300 nm p-type PbS layer doped at  $N_a = 10^{17} \text{ cm}^{-3}$  and  $N_d = 10^{14} \text{ cm}^{-3}$ . Note that the P(VDF-TrFE) to holes aspect ratio (33/84) has been chosen to match the experimental conditions. The COMSOL semiconductor module

solving for the Poisson equation and continuity equations was then used to calculate the short circuit current density ( $J_{sc}$ ). Other materials parameters used for the calculation are reported in the simulation parameters table below.

Simulation Parameters Table

Parameters	ZnO	PbS QDs
Relative permittivity ( $\epsilon$ )	66	20
Band Gap (eV)	3.2	1.3
Electron Affinity (eV)	4.3	3.9
Effective Density of states, Conduction band ( $\text{cm}^{-3}$ )	1.00E+19	1.00E+19
Effective Density of states, Valence band ( $\text{cm}^{-3}$ )	1.00E+19	1.00E+19
Electron Mobility ( $\text{cm}^2\text{V}^{-1}\text{s}^{-1}$ )	5.00E-02	2.00E-02
Hole Mobility ( $\text{cm}^2\text{V}^{-1}\text{s}^{-1}$ )	5.00E-02	2.00E-02

The strain dependent polarization  $\sigma$  obtained in step 1 was then applied at the ZnO/P(VDF-TrFE) interfaces as well as with an opposite sign at the P(VDF-TrFE)/PbS interfaces using a surface charge density boundary condition, which is similar to previous approaches.[3] To perform the  $J_{sc}$  calculations, a generation term under AM1.5G was calculated using the SCAPS software with absorption values for PbS QDs taken from the literature [4], and added to the continuity equations in COMSOL. Likewise, band to band and Auger recombination were considered in the PbS QD layers and added to the model as follows:

$$R_{band} = b(np - n_i^2),$$

$$R_{auger} = (np - n_i^2)(\Gamma_n n + \Gamma_p p),$$

where  $n_i$  is the intrinsic concentration,  $n$  and  $p$  the electron and hole concentration, respectively,  $b$  the radiative recombination coefficient of  $5 \times 10^{-13} \text{ cm}^3\text{s}^{-1}$ , and  $\Gamma_n$ ,  $\Gamma_p$  the auger coefficient of electrons and holes taken to be  $1 \times 10^{-28} \text{ cm}^3\text{s}^{-1}$ . [5] Hole and electron currents under light illumination are then obtained by solving the continuity equations:

$$\begin{cases} \frac{1}{q} \nabla \cdot J_n = -G_{1.5} + R_{band} + R_{auger} \\ -\frac{1}{q} \nabla \cdot J_p = -G_{1.5} + R_{band} + R_{auger} \end{cases}$$

The short circuit current density is obtained by summing up these two quantities,  $J_{sc} = J_n + J_p$ .

**Supporting Information II. Theories and equations.****1. Electric potential distribution at a p-n junction.[6]**

$$\varphi(x) = \begin{cases} V_{bi}, & \text{for } x \leq -w_n \\ V_{bi} - \frac{qN_D(x+w_n)^2}{2\varepsilon_r}, & \text{for } -w_n \leq x \leq 0 \\ \frac{qN_A(x-w_p)^2}{2\varepsilon_r}, & \text{for } 0 \leq x \leq w_p \\ 0, & \text{for } x \geq w_p \end{cases} \quad (1)$$

where  $\varphi(x)$  is an electric potential profile across the junction,  $V_{bi}$  built-in potential,  $\varepsilon_r$  the relative permittivity of the semiconducting materials. Due to the piezoelectric potential, the space charge region was decreased when a QDSC was subjected to compressive strain whereas the depletion width was increased when the QDSC was subjected to a tensile strain as shown in Figure 3. Consequently, the electric potential at the junction was increased due to a decrease in the space charge region under compressive strain. On the contrary, the electric potential at the junction was decreased due to an increase in the space charge region for tensile strain, which is in good agreement with the above equation (1).

**2. Exciton dissociation rates ( $K_d$ ).[7,8]**

$$K_d = \frac{3R}{4\pi a^3} e^{-E_B/k_B T} \left( 1 + b + b^2/3 + \dots \right), \quad b = b^3 E / 8\pi \varepsilon_0 \varepsilon K^2 T^2 \quad (2)$$

where  $R$  is the bimolecular rate constant of the bound electron-hole (e-h) pair,  $a$  the initial separation of the bound e-h pair at the interface charge transfer exciton,  $E_B$  the e-h pair's binding energy, and  $k_B$  the Boltzmann constant. Equation (2) describes that exciton dissociation rates are dependent on the strength of the electric potential that is stronger than the e-h binding energy,  $E_B$ , so as to effectively dissociate e-h pairs.

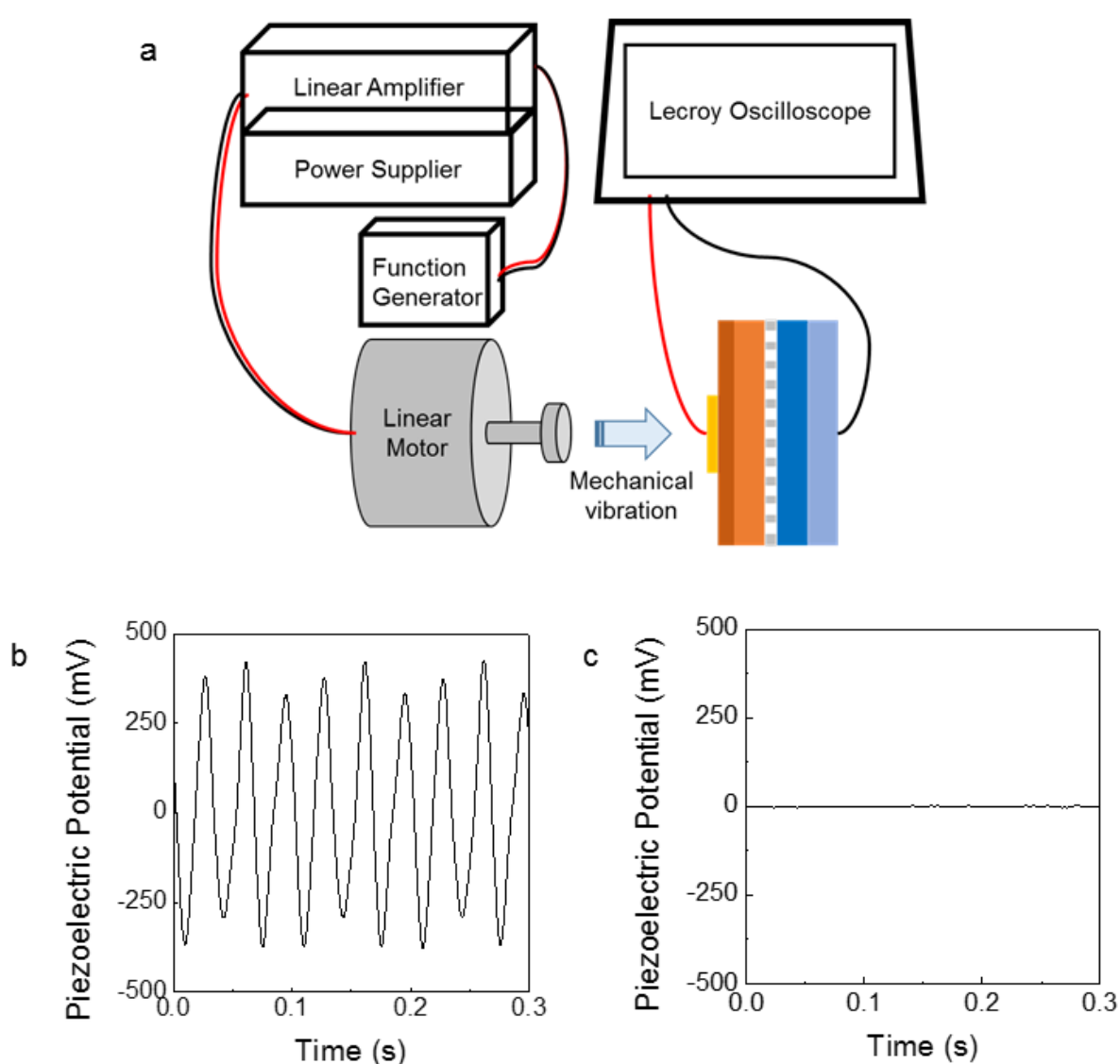
**3. Ideality factor ( $n$ ) calculation.[9]**

$$I = I_s \left[ \exp\left(\frac{qV}{nk_B T}\right) - 1 \right] \quad (3)$$

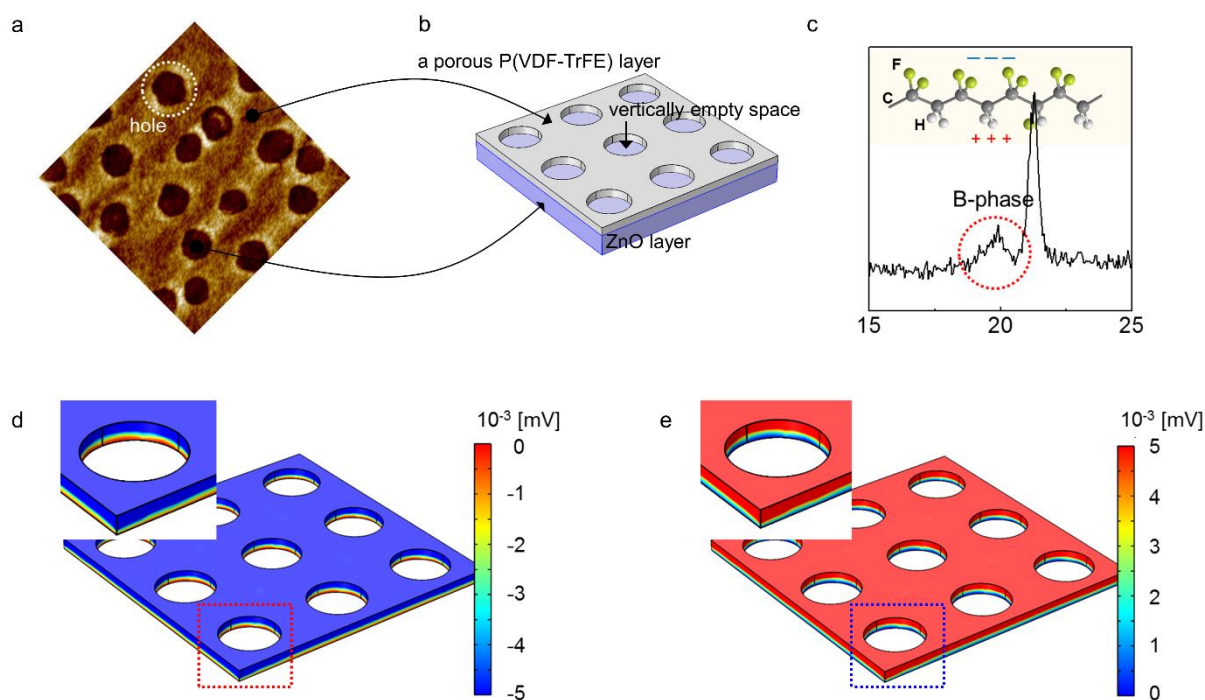
where  $I_s$  is dark saturation current,  $n$  the ideality factor which depends on the recombination mechanism and  $k_B T/q$  was set to 25.86 mV (room temperature) for the calculation. The Ideality factor was calculated by fitting the dark I-V curves with the ideal diode equation (3). An ideality factor ( $n$ ) close to unity indicates a trap-free recombination whereas  $n$  close to 2 indicates that a trap-assisted recombination is dominant.

**Supporting Information III. Piezoelectric Potential Measurement.**

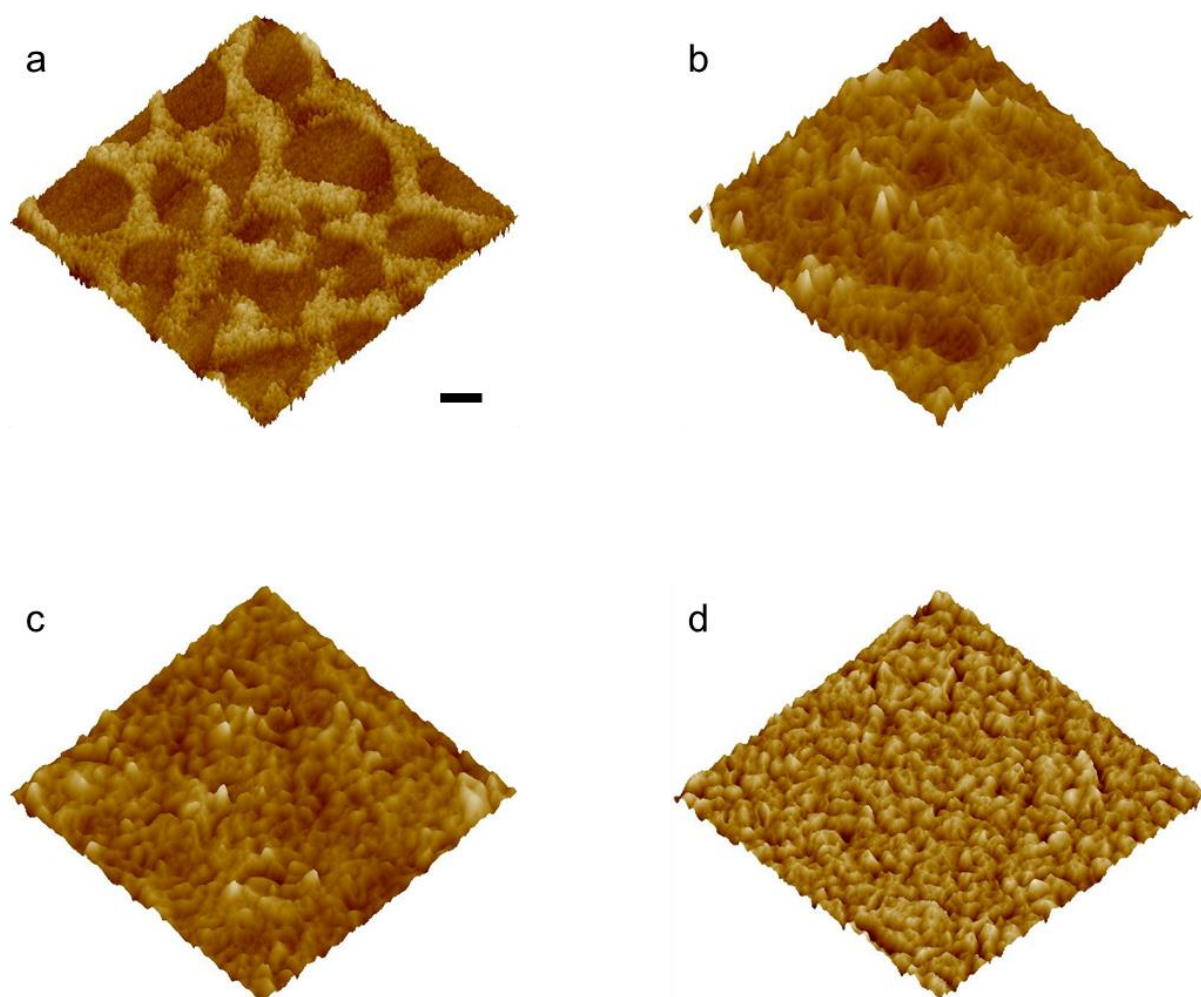
To measure the piezoelectric potential generated by the P(VDF-TrFE) layer in the flexible PbS QDSC (Au/ EDT/ TBAI/ porous P(VDF-TrFE)/ ZnO/ ITO or Au/ EDT/ TBAI/ ZnO/ ITO), we assembled the measurement set-up as shown in Supplementary Schematics 1. Mechanical vibrations at a frequency of 30 Hz, generated by a function generator, were applied to the flexible PbS QDSC. Following this, the piezoelectric potential was then read by an oscilloscope (Lecroy).



**Supplementary Figure S1.** (a) Schematic of the piezoelectric potential measurement system. (b) Measured piezoelectric potential from the QDSC with a ZnO-porous P(VDF-TrFE) layer and (c) Measured piezoelectric potential from the QDSC with only ZnO layer.



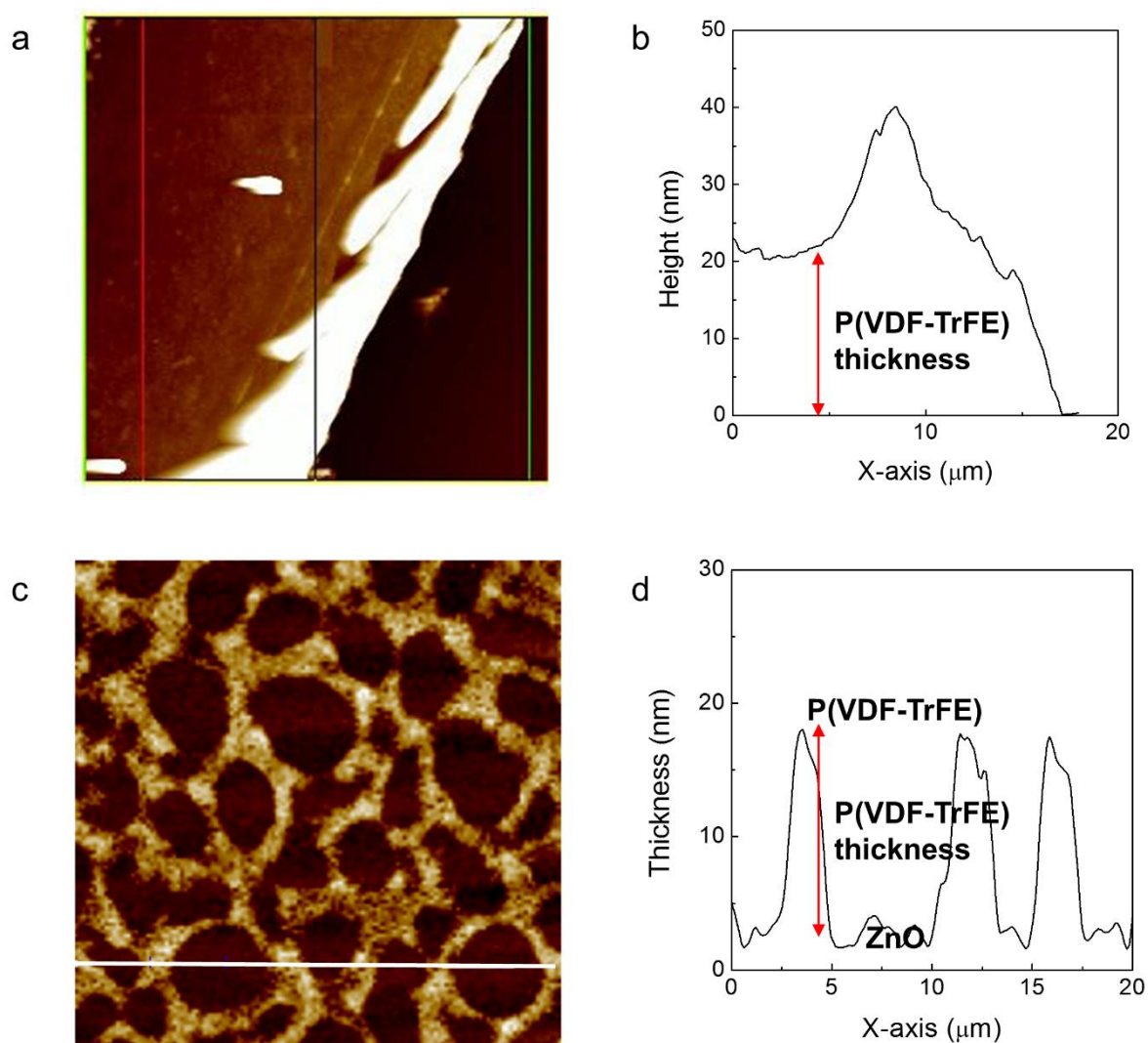
**Supplementary Figure S2.** (a) 3D AFM image of a porous P(VDF-TrFE) layer. (b) Schematics of a porous P(VDF-TrFE) structure on the ZnO layer in (a). (c) Measured XRD peak from the ZnO-porous P(VDF-TrFE) layer and molecular structure of the  $\beta$ -phase P(VDF-TrFE) polymer where the fluorine atoms exhibit negative charge and hydrogen atoms exhibit a positive charge. (d) COMSOL Simulation results on the generation of an electric field by the porous P(VDF-TrFE) layer with respect to tensile (left) and compressive (right) strain.



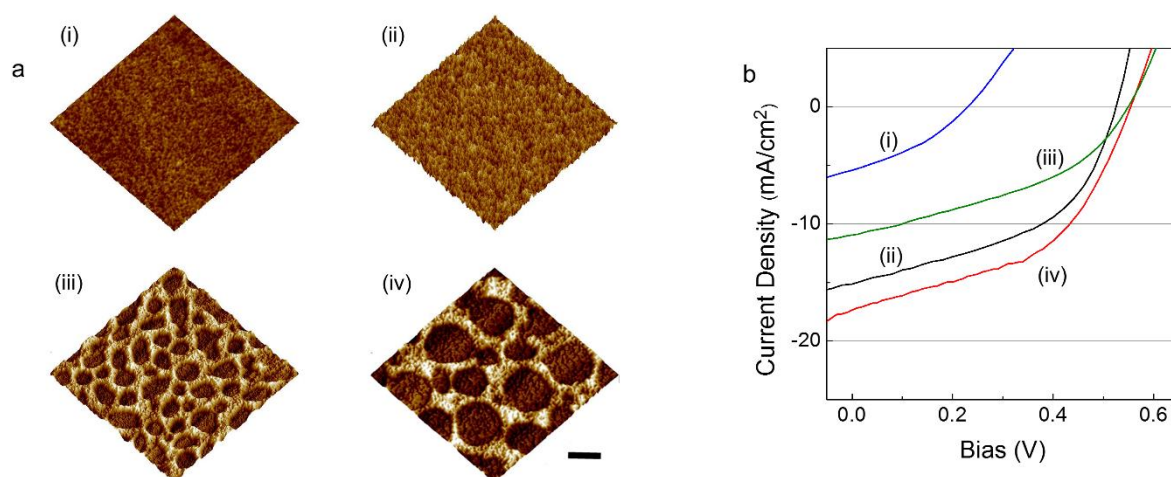
**Supplementary Figure S3.** The evolution of the morphology of a porous P(VDF-TrFE) layer following the deposition of QDs: (a) a ZnO-porous P(VDF-TrFE) layer, (b) 1 layer of QDs on the ZnO-porous P(VDF-TrFE) layer, (c) 3 layers of QDs on the ZnO-porous P(VDF-TrFE) layer, and (d) 12 layers of QDs on only a ZnO layer (Scale bar: 1  $\mu\text{m}$ ).

**Supplementary Table S1.** Parameters of the flexible QDSCs shown in Figure 4a and b.

Figure	Strain (%)	$V_{oc}$ (V)	$J_{sc}$ (mAcm <sup>-2</sup> )	$R_s$ ( $\Omega$ cm <sup>2</sup> )	$R_{sh}$ ( $\Omega$ cm <sup>2</sup> )	FF	PCE (%)
Figure 4(a)-blue	0	0.24	5.41	15.16	47.29	0.34	<b>0.44</b>
Figure 4(a)-red	0	0.55	17.41	10.02	107.00	0.47	<b>4.30</b>
Figure 4(b)	Compressive 1.25	0.55	19.53	8.88	118.67	0.47	<b>5.04</b>
	Compressive 1.20	0.55	18.54	8.66	115.92	0.48	<b>4.92</b>
	Compressive 1.15	0.55	18.28	8.79	112.31	0.48	<b>4.83</b>
	Compressive 1.10	0.55	17.83	8.44	114.01	0.48	<b>4.71</b>
	0	0.55	17.41	10.02	107.00	0.47	<b>4.30</b>
	Tensile 1.10	0.54	15.68	13.78	103.69	0.47	<b>4.00</b>
	Tensile 1.15	0.54	15.22	12.62	107.30	0.47	<b>3.91</b>
	Tensile 1.20	0.54	14.66	13.07	107.20	0.47	<b>3.79</b>
	Tensile 1.25	0.54	14.26	12.14	108.21	0.47	<b>3.68</b>



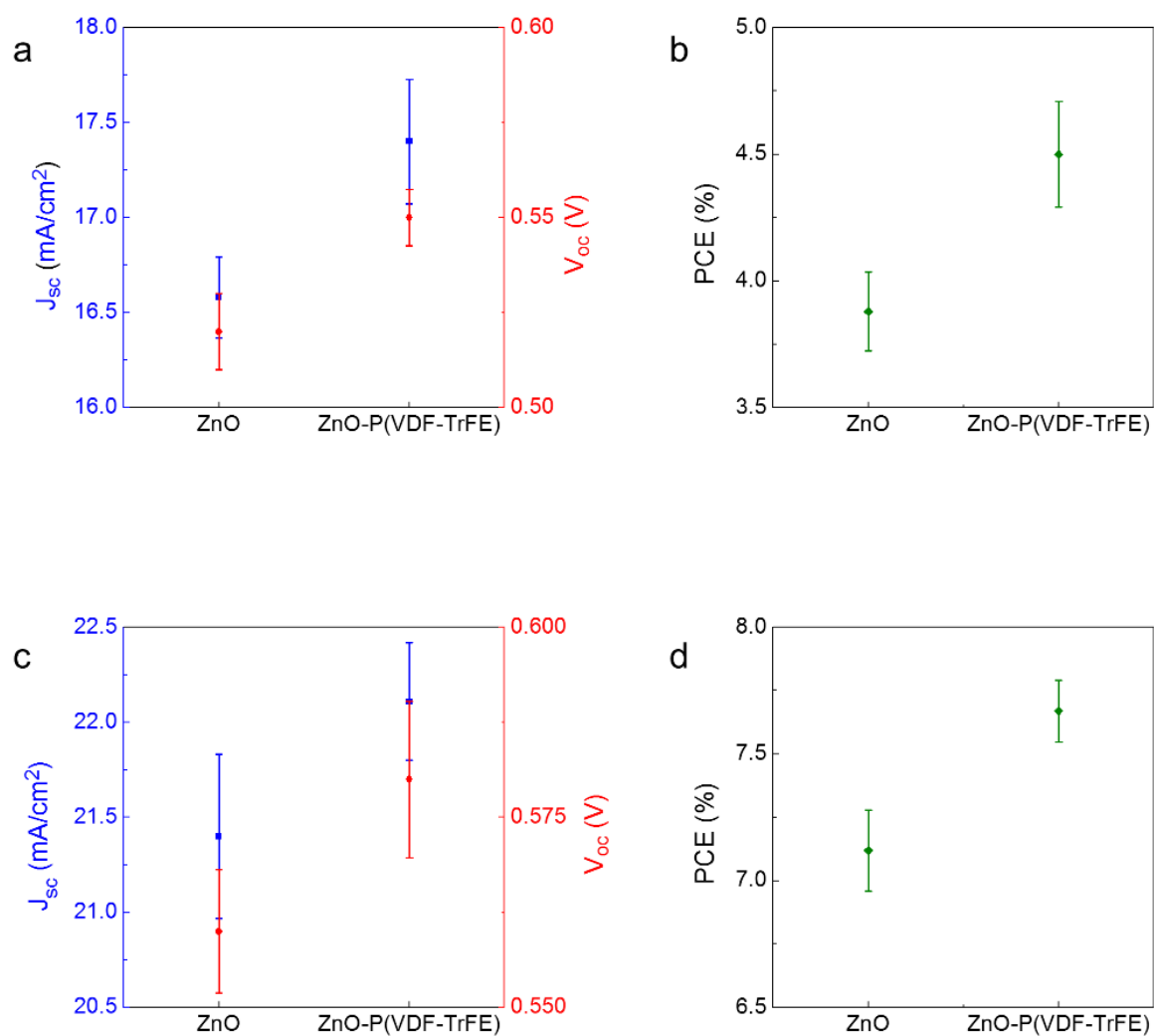
**Supplementary Figure S4.** (a) and (b) AFM images and analyzed thickness of a non-porous P(VDF-TrFE) layer, respectively. (c) and (d) AFM images and analyzed thickness of a porous P(VDF-TrFE) layer, respectively, where the white line indicates the cross-section where the height profile was read.



**Supplementary Figure S5.** (a) 3D AFM images of (i) a non-porous P(VDF-TrFE) layer (ii) only a ZnO layer, and (iii) and (iv) a porous P(VDF-TrFE) layer (Scale bar: 1  $\mu\text{m}$  for (i), (ii), (iii) and 2  $\mu\text{m}$  for (iv)). (b) Performances of the QDSCs with respect to the different porous P(VDF-TrFE) layers shown in (a).

**Supplementary Table S2.** Parameters of the QDSCs in Supplementary Figure S5.

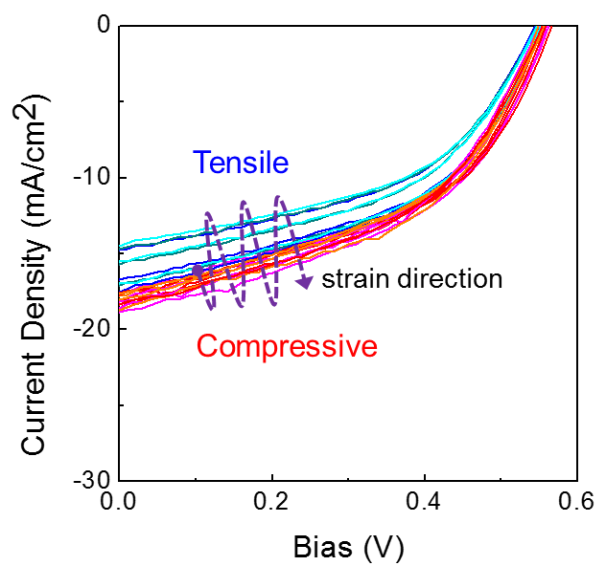
Sample	Device structure	$V_{oc}$ (V)	$J_{sc}$ (mAcm <sup>-2</sup> )	FF	PCE (%)
(a)-(i)	ZnO-non-porous P(VDF-TrFE)	0.24	5.41	0.34	<b>0.44</b>
(a)-(ii)	Only ZnO	0.52	15.13	0.47	<b>3.69</b>
(a)-(iii)	ZnO- porous P(VDF-TrFE)	0.55	11.37	0.40	<b>2.50</b>
(a)-(iv)	ZnO- porous P(VDF-TrFE)	0.55	16.74	0.47	<b>4.32</b>



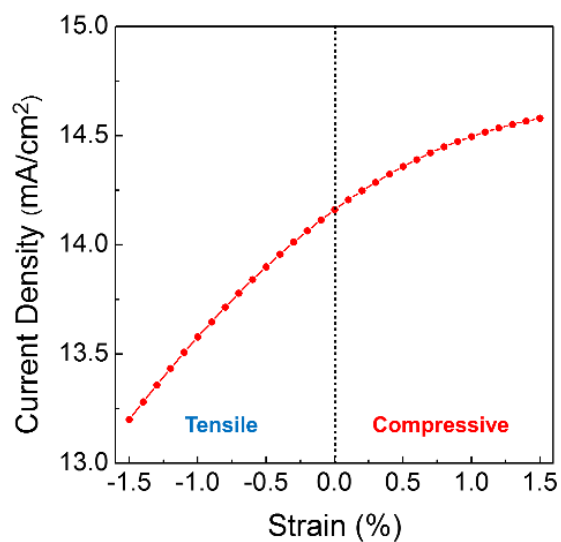
**Supplementary Figure S6.** Comparison of the performance of PbS QDSCs with only a ZnO layer (Black) and a porous P(VDF-TrFE) layer (Red) on (a and b) a flexible substrate (c and d) a glass substrate for no applied strain.

**Supplementary Table S3.** Average value (9 devices) of the QDSC parameters shown in Supplementary Figure S6.

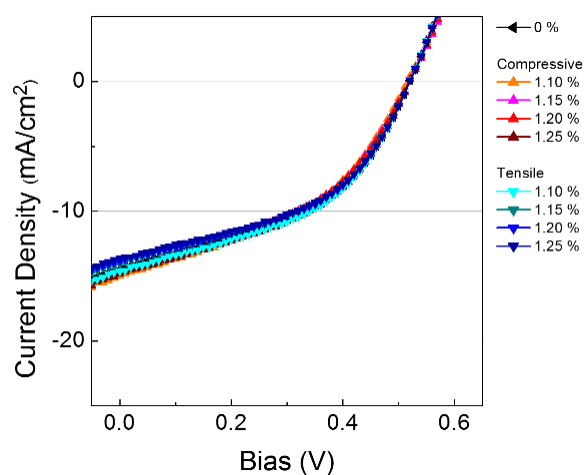
Sample	QDSC structure	$V_{oc}$ (V)	$J_{sc}$ (mAcm <sup>-2</sup> )	FF	PCE (%)
Figure S6(a)-(i)	Only ZnO-TBAI 10L/ EDT 2L	$0.52 \pm 0.0100$	$16.58 \pm 0.2135$	$0.45 \pm 0.0128$	$3.88 \pm 0.1560$
Figure S6(a)-(i)	ZnO-P(VDF-TrFE)-TBAI 10L/ EDT 2L	$0.55 \pm 0.0074$	$17.40 \pm 0.3274$	$0.47 \pm 0.0250$	$4.50 \pm 0.2076$
Figure S6(b)-(i)	Only ZnO-TBAI 10L/ EDT 2L	$0.56 \pm 0.0081$	$21.40 \pm 0.4316$	$0.59 \pm 0.0093$	$7.12 \pm 0.1593$
Figure S6(b)-(ii)	ZnO-P(VDF-TrFE)-TBAI 10L/ EDT 2L	$0.58 \pm 0.0103$	$22.11 \pm 0.3090$	$0.60 \pm 0.0146$	$7.67 \pm 0.1211$



**Supplementary Figure S7.** The reversible performance of a QDSC when the device was subjected to repeated compressive and tensile strain.



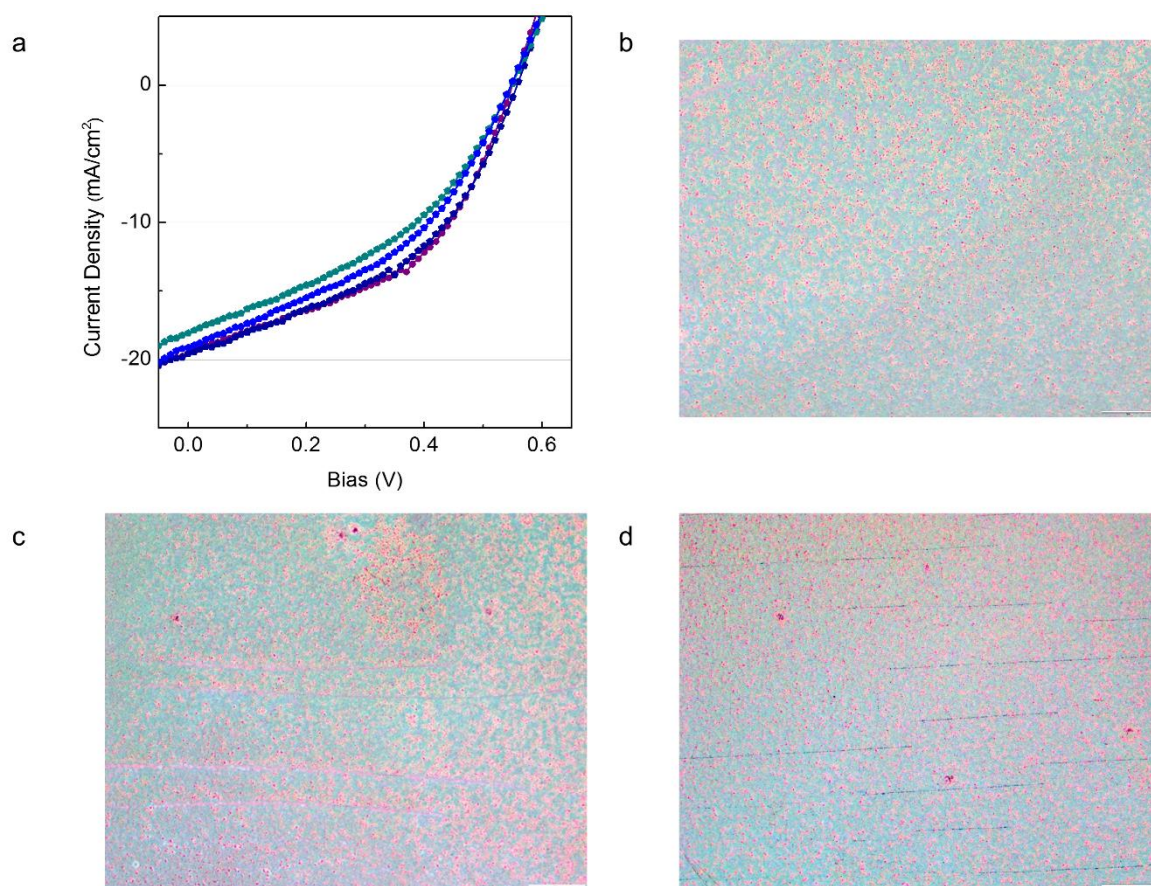
**Supplementary Figure S8.** Modulation of the  $J_{sc}$  level when tensile and compressive strain were applied to the devices, which was simulated using the COMSOL Multiphysics software.



**Supplementary Figure S9.** Negligible performance changes upon the application of compressive or tensile strain on the flexible PbS QDSC consisting of only a ZnO layer. Supplementary Table S4 shows the average QDSC parameters.

**Supplementary Table S4.** Average value of QDSC parameters with only a ZnO layer extracted from Supplementary Figure S9.

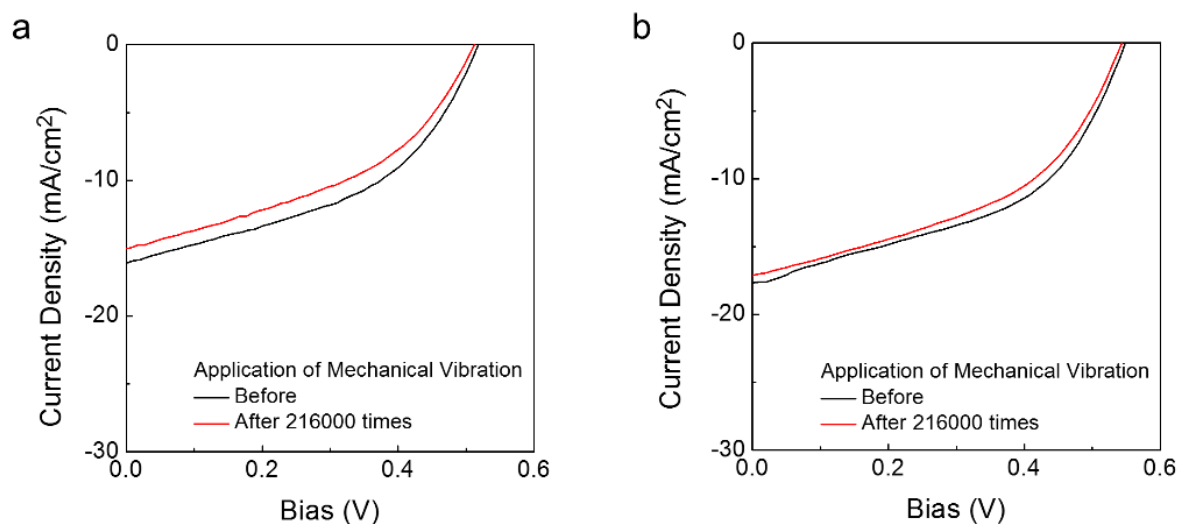
Sample	Strain (%)	$V_{oc}$ (V)	$J_{sc}$ (mAcm <sup>-2</sup> )	FF	PCE (%)
Supplementary Figure S9	Compressive 1.25	$0.52 \pm 0.0070$	$-16.55 \pm 0.6588$	$0.44 \pm 0.0078$	$3.80 \pm 0.0907$
	Compressive 1.20	$0.52 \pm 0.0058$	$-16.49 \pm 0.7911$	$0.44 \pm 0.0078$	$3.75 \pm 0.1193$
	Compressive 1.15	$0.52 \pm 0.0050$	$-16.70 \pm 0.1913$	$0.44 \pm 0.0080$	$3.80 \pm 0.0964$
	Compressive 1.10	$0.52 \pm 0.0058$	$-16.96 \pm 0.0919$	$0.44 \pm 0.0104$	$3.85 \pm 0.1081$
	0	$0.52 \pm 0.0058$	$-16.65 \pm 0.6945$	$0.44 \pm 0.0152$	$3.79 \pm 0.0611$
	Tensile 1.10	$0.52 \pm 0.0010$	$-16.71 \pm 0.7120$	$0.43 \pm 0.0174$	$3.77 \pm 0.0945$
	Tensile 1.15	$0.52 \pm 0.0050$	$-16.10 \pm 1.0772$	$0.44 \pm 0.0180$	$3.75 \pm 0.1050$
	Tensile 1.20	$0.52 \pm 0.0083$	$-16.47 \pm 0.8318$	$0.44 \pm 0.0176$	$3.76 \pm 0.1253$
	Tensile 1.25	$0.52 \pm 0.0072$	$-16.03 \pm 0.5139$	$0.44 \pm 0.0207$	$3.69 \pm 0.17$



**Supplementary Figure S10.** (a) Performance of a QDSC with a porous P(VDF-TrFE) layer at compressive strains 1.25 (purple), 1.3 (navy), 1.35 (blue), and 1.4% (light blue), respectively. Microscope images were taken at strains of (b) 1.25%, (c) 1.3%, and (d) 1.4%. The solar cell parameters are shown in Supplementary Table S5.

**Supplementary Table S5.** Solar cell parameters corresponding to Supplementary Figure S10.

Sample	Strain (%)	$V_{oc}$ (V)	$J_{sc}$ (mAcm <sup>-2</sup> )	FF	PCE (%)
Figure S10	Compressive 1.25	0.55	19.53	0.47	5.04
	Compressive 1.30	0.55	19.55	0.44	4.85
	Compressive 1.35	0.55	19.12	0.41	4.27
	Compressive 1.40	0.55	18.08	0.39	3.92



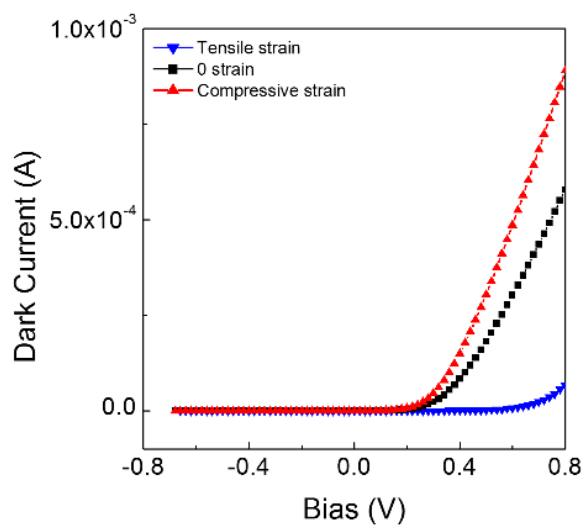
**Supplementary Figure S11.** Stability of (a) QDSC with only a ZnO layer and (b) QDSC with a ZnO-porous P(VDF-TrFE) layer after the application of mechanical vibrations for 2 hours by a linear motor (Supplementary Figure S1).

**Supplementary Table S6.** Parameters of the QDSCs shown in Supplementary Figure S11.

Sample	Note	$V_{oc}$ (V)	$J_{sc}$ (mAcm <sup>-2</sup> )	FF	PCE (%)
Only ZnO	Before application of mechanical vibrations	0.518	16.12	0.45	<b>3.74</b>
	After application of mechanical vibrations	0.510	15.07	0.43	<b>3.32</b>
ZnO-porous P(VDF-TrFE)	Before application of mechanical vibrations	0.550	17.59	0.47	<b>4.59</b>
	After application of mechanical vibrations	0.543	17.03	0.46	<b>4.25</b>

**Supplementary Table S7.** Calculated ideality factor from a QDSC with porous P(VDF-TrFE) layer in Supplementary Figure S12 according to equation (3) in Supplementary Information II.

Sample	Strain (%)	n
Figure S12	Compressive 1.25	1.755
	0	1.823
	Tensile 1.25	2.927



**Supplementary Figure S12.** Measured dark current at 0% strain (Black), Tensile 1.25% (Blue), and Compressive 1.25% (Red).

## References

- [1] J. Tarn, L. Huang, *Int. J. Solids Struct.* **2002**, 39, 4979.
- [2] K. Omote, H. Ohigashi, K. Koga, *J. Appl. Phys.* **1997**, 81, 2760.
- [3] K. Shin, T. Y. Kim, G. C. Yoon, M. K. Gupta, S. K. Kim, W. Seung, H. Kim, S. Kim, S. Kim, S. Kim, *Adv. Mater.* **2014**, 26, 5619.
- [4] B. T. Diroll, E. A. Gaulding, C. R. Kagan, C. B. Murray, *Chem. Mater.* **2015**, 27, 6463.
- [5] X. Lan, O. Voznyy, A. Kiani, F. P. García de Arquer, A. S. Abbas, G.-H. Kim, M. Liu, Z. Yang, G. Walters, J. Xu, M. Yuan, Z. Ning, F. Fan, P. Kanjanaboos, I. Kramer, D. Zhitomirsky, P. Lee, A. Perelgut, S. Hoogland, E. H. Sargent, *Adv. Mater.* **2016**, 28, 299.
- [6] S. Dimitrijević, *Principles of semiconductor devices*, Oxford University Press **2012**.
- [7] Y. Yuan, T. J. Reece, P. Sharma, S. Poddar, S. Ducharme, A. Gruverman, Y. Yang, J. Huang, *Nat. Mater.* **2011**, 10, 296.
- [8] K. S. Nalwa, J. A. Carr, R. C. Mahadevapuram, H. K. Kodali, S. Bose, Y. Chen, J. W. Petrich, B. Ganapathysubramanian, S. Chaudhary, *Energy Environ. Sci.* **2012**, 5, 7042.
- [9] C. M. Chuang, A. Maurano, R. E. Brandt, G. W. Hwang, J. Jean, T. Buonassisi, V. Bulović, M. G. Bawendi, *Nano Lett.* **2015**, 15, 3286.